

Article

Microstructure and High Temperature-Mechanical Properties of TiC/Graphene/Ti6Al4V Composite Formed by Laser Powder Bed Fusion

Shijie Chang ¹, Wenbo Du ^{2,*}, Zhanyong Zhao ^{1,*}  and Peikang Bai ¹¹ School of Materials Science and Engineering, North University of China, Taiyuan 030051, China² National Key Laboratory for Remanufacturing, Academy of Army Armored Forces, Beijing 100072, China

* Correspondence: dwbneu@163.com (W.D.); zhaozy@nuc.edu.cn (Z.Z.); Tel.: +86-136-2346-6690 (Z.Z.)

Abstract: TiC/graphene/Ti6Al4V composites were prepared by laser powder bed fusion using graphene and Ti6Al4V powder. The differences in microstructure and high-temperature mechanical properties between the Ti6Al4V alloy and the TiC/graphene/Ti6Al4V composite were studied. The tensile and microhardness of the two materials were tested at 400 °C, 500 °C, and 600 °C; the results of the TiC/graphene/Ti6Al4V composite were 126 MPa, 162 MPa, and 76 MPa and 70 HV, 59 HV, and 61HV, respectively, higher than those of the Ti6Al4V alloy. These results happened because graphene reacted with Ti to form TiC particles, which were homogeneously distributed amongst α' acicular martensite. The addition of graphene refined the size of the acicular α' martensite. At the same time, the graphene and TiC particles showed a dispersion-strengthening effect. The mechanical properties of the TiC/graphene/Ti6Al4V composite were improved by the combination of fine-grain strengthening and dispersion strengthening mechanisms.

Keywords: laser powder bed fusion; graphene; high temperature; mechanical property



Citation: Chang, S.; Du, W.; Zhao, Z.; Bai, P. Microstructure and High Temperature-Mechanical Properties of TiC/Graphene/Ti6Al4V Composite Formed by Laser Powder Bed Fusion. *Metals* **2023**, *13*, 163. <https://doi.org/10.3390/met13010163>

Academic Editors: Milan Brandt and Aleksander Lisiecki

Received: 20 October 2022

Revised: 8 January 2023

Accepted: 11 January 2023

Published: 12 January 2023



Copyright: © 2023 by the authors. Licensee MDPI, Basel, Switzerland. This article is an open access article distributed under the terms and conditions of the Creative Commons Attribution (CC BY) license (<https://creativecommons.org/licenses/by/4.0/>).

1. Introduction

Titanium alloy has the advantages of high specific and thermal strength, strong corrosion resistance, and good process performance, and it has become an ideal engineering structural material in aerospace, chemical, and other fields [1]. The Ti6Al4V alloy can work at a temperature of 400 °C for a long time and is mainly used to manufacture fans, compressor disks, and engine blades in the aviation industry [2]. However, with the development of the new generation of aerospace technology, the high-temperature properties of the Ti6Al4V alloy no longer meet the requirements, whereas titanium matrix composites have become candidate materials for applications in high-speed aerospace vehicles and new aeroengines [3,4]. Because ceramic particles have high hardness, high wear resistance, and high-temperature performance, they are widely used to manufacture titanium matrix composites, such as TiC [5], WC [6], and TiB [7]. In recent years, because of its unique electrical, mechanical, and thermal properties, graphene has become an ideal reinforcement material for preparing lightweight, high-strength, and high-performance metal matrix composites [8]. For example, Guo et al. [9] developed the Ni-P@GNFs/Ti6Al4V composite. The compressive strength of the composite reached 1133 MPa, an increase of 30.6% compared to that of Ti6Al4V (867 MPa). Shang et al. [10] also used plasma sintering to prepare multi-layer graphene and Ti6Al4V-based discontinuous reinforced composite that reached a tensile strength of 1010 MPa [10].

Laser powder bed fusion (LPBF) is a powder bed melting additive manufacturing (AM) technology that forms parts by layer-by-layer selective melting and layer-by-layer superposition [10,11]. Based on the forming characteristics, LPBF technology can integrate parts with complex structures, shorten the product development cycle, and improve the utilization of materials [12,13]. In recent years, LPBF technology has been widely used in

medical, dental, and especially aerospace fields [14], and the parts formed with porous structures have reduced weight [15]. Although LPBF technology has many advantages, there are still some defects such as pores and residual stress; hence, the quality of products can be improved by adjusting the printing parameters to control such defects [16–18], especially by combining large data acquisition and analysis with the printing process [19]. With the use of LPBF technology, graphene-reinforced metal matrix materials can significantly improve the performance of composites. Zhao et al. [20] used an organic aluminum reduction method to coat graphene with a nano aluminum layer and used LPBF technology to prepare aluminum-coated graphene/AlSi10Mg alloy matrix composites and the nano-scale Al₄C₃ precipitates generated in the composite. The tensile strength and hardness of the composite increased by 11% and 40.8%, respectively. Wang et al. [21] used the LPBF technology to prepare a graphene/Inconel 718 composite, and the tensile strength and Young's modulus of the composite reached 1511 MPa and 675 GPa, respectively [21].

Previous studies have used LPBF technology to enhance Ti6Al4V alloys with graphene, which exhibits excellent mechanical properties at room temperature [22–24]. However, the high-temperature mechanical properties of TiC/Ti6Al4V composites have rarely been reported. In this study, the TiC/graphene/Ti6Al4V composites were prepared by the LPBF method using Ti6Al4V alloy powder and graphene powder as raw materials. The purpose of this study was to explore the differences between the microstructure and high-temperature mechanical properties of the LPBF-formed Ti6Al4V alloy and the TiC/graphene/Ti6Al4V composite to reveal the strengthening mechanism of the composite.

2. Materials and Methods

The raw material for preparing the composite materials was Ti6Al4V alloy powder provided by Zhonghang Maite Powder Metallurgy Technology Co. Ltd. (Beijing, China). The particle size distribution of the powder was D10 = 19.9 μm , D50 = 35.4 μm , D90 = 58 μm . The powder material composition, provided by the company, is shown in Table 1. Note that 0.3-wt% graphene was added to the composite materials. The graphene powder was provided by KENA Carbon New Materials Co. Ltd. (Lanzhou, China), and the graphene morphology is shown in Figure 1a.

Table 1. Chemical composition of Ti6Al4V Powder.

Ti	Al	V	Fe	C	N	H	O	Si
bal	5.5~6.5	3.5~4.5	≤ 0.25	≤ 0.08	≤ 0.03	≤ 0.012	≤ 0.1	< 0.15

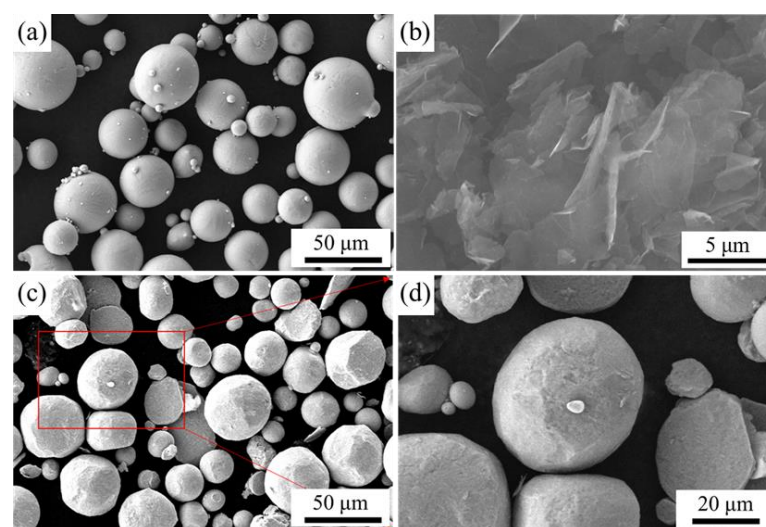


Figure 1. (a) Ti6Al4V powder morphology; (b) graphene morphology; (c,d) morphology of graphene and Ti6Al4V powder after ball milling.

A planetary ball mill (QM-3SP4 model) was adopted. The ball milling parameters were as follows: the specific gravity between the weight of the ball and the weight of the composite powder was 8:1; the ball milling time was 3 h; and the ball milling speed was 240 rad/min. The mixed powder is shown in Figure 1 b. The metal 3D printing equipment of Easy 3D EP-M150 was used, and the two materials used the same printing process parameters. The process parameters used were as follows: laser power of 200 W, scanning spacing of 0.12 mm, powder layer thickness of 0.03 mm, and scanning speed of 1200 mm/s; a checkerboard scanning strategy was adopted, and each layer was rotated by 67°. The substrate was preheated to 120 °C. The sample forming building direction is shown in Figure 2a.

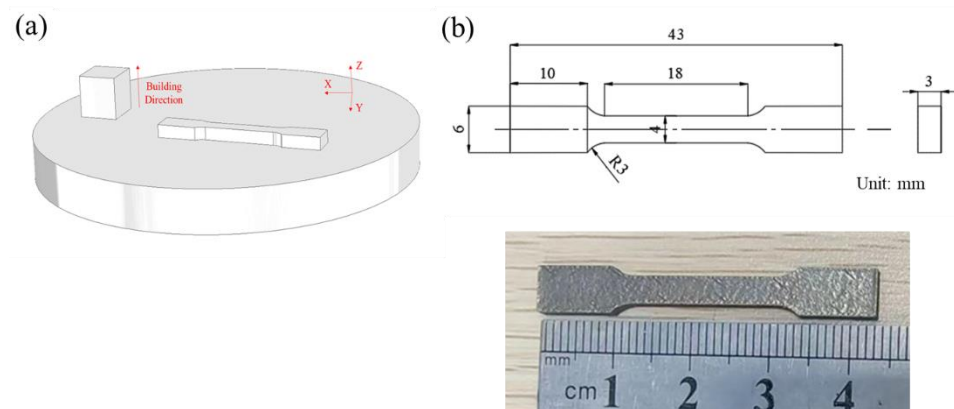


Figure 2. (a) Schematic of building direction; (b) tensile specimen.

An MH-300A electronic densitometer was used to measure the density of the samples. Five samples of each material were measured, and the average value ρ_s was taken. The density value was calculated as $\rho_s / \rho_n * 100$. The ρ_n is the standard density of Ti-x vol.% graphene, and the density of Ti6Al4V is 4.5g/cm³. The HGW-300G microcomputer-controlled high-temperature material tensile testing machine was used to raise the temperature of the sample to 400 °C, 500 °C, and 600 °C at a rate of 10 °C/s and to keep it stable for 5 min. The tensile rate was set as 0.5 mm/min. The experiment was repeated three times and the average value was used. The size of the tensile sample is shown in Figure 2b. Thereafter, the ZD-HVZHT-30 high-temperature Vickers hardness tester was used to raise the temperature of the sample to 400 °C, 500 °C, and 600 °C at a heating rate of 10 °C/s, and to keep it stable for 5 min. A diamond indenter with a load of 4.904 N (500 g) was used for 10 s. Five points were randomly selected on the polished sample surface for the measurements, and the average values of these five measurements were considered.

Next, the standard polished parts were placed in a 5 mL HF, 25 mL HNO₃, and 50 mL H₂O corrosion solution for etching for 30–35 s. A field emission scanning electron microscope (SEM; JSM-7900F, JEOL, Peabody, MA, USA) was used to observe the structure of the sample with a working voltage set to 10.0 KV. The preparation of the TEM sample was as follows: First, the sample was cut into 0.5 mm thick sheets with a wire cutting machine, and the sheets were ground to 35~40 μm with 1000 # SiC water abrasive paper thick. Then, the sheet was punched into a round shape with a diameter of 3 mm. Finally, a Gatan-691 precision argon ion instrument was used for thinning. TEM samples were characterized by field emission transmission electron microscopy (JEM-2100F) with an acceleration voltage of 200kV.

3. Results and Discussion

3.1. Initial Microstructure

Figure 3 shows the microstructure of the Ti6Al4V alloy and graphene-reinforced Ti6Al4V composite. A large amount of coarse α' acicular martensite was observed. The α' acicular martensite was refined, as shown in Figure 3. New nanoparticles were formed in

the graphene-reinforced Ti6Al4V composite, as shown in Figure 3d. According to the EDS analysis (Figure 3f), the granular precipitation was mainly composed of Ti and C elements, and the atomic ratio was close to 1:1. Figure 3d shows the TEM micromorphology and selected area electron diffraction (SAED) (Figure 3e) of TiC particles. Previous studies have also verified the existence of graphene [25] and TiC (Figure 4 [26]). In general, the reinforcing phases in the graphene-reinforced Ti6Al4V composite are graphene and TiC particles.

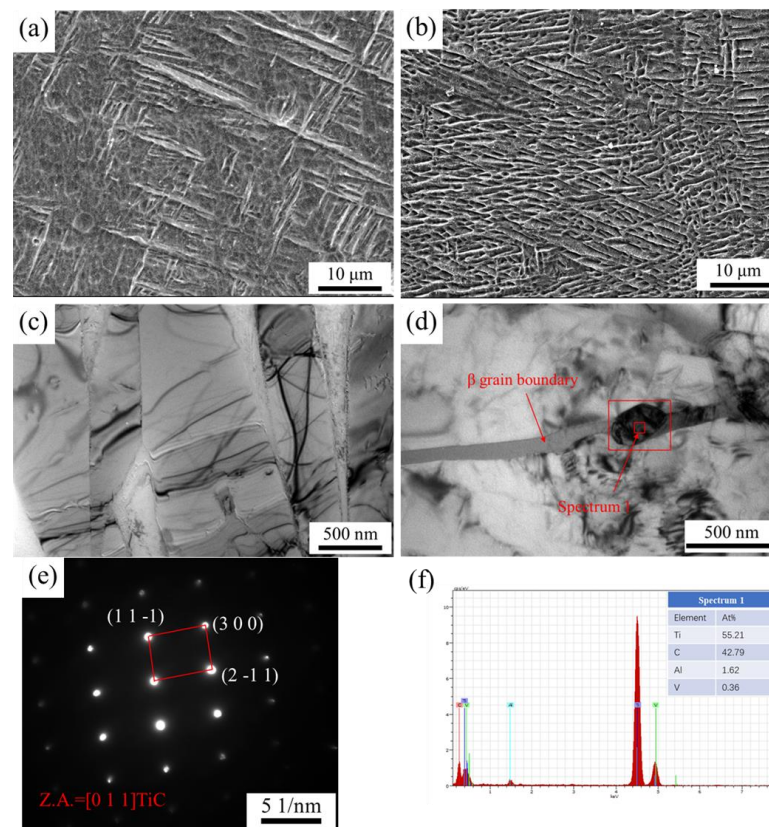


Figure 3. (a) SEM image of the longitudinal section of the Ti6Al4V alloy; (b) SEM images of the graphene reinforced Ti6Al4V composite; (c) TEM morphology of the Ti6Al4V alloy; (d) TEM morphology of the graphene reinforced Ti6Al4 V composite; (e) SAED figure of the selected area in (d); (f) composition analysis at point 1.

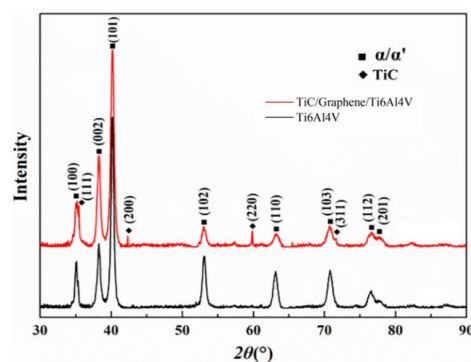


Figure 4. XRD patterns of the TiC/graphene/Ti6Al4V composite and Ti6Al4V alloy. Reprinted with permission from Ref. [26]. 2023, Elsevier.

Figure 5 shows the micro morphologies of the Ti6Al4V alloy and composite at a lower magnification under SEM, where no pores were observed, while a small number of pores with a diameter of $5 \mu\text{m}$ were observed in the composite. The density of the

Ti6Al4V alloy was 99.2%, and that of the TiC/graphene/Ti6Al4V composite was 98.9%. Therefore, the porosity of the formed composite material was more than that of the Ti6Al4V alloy; however, a density above 98% had little influence on its mechanical properties [27]. Therefore, the influence of porosity on the formation of voids during tension is lower.

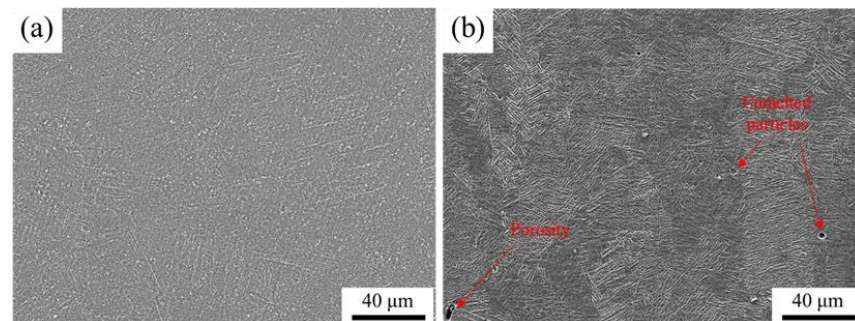


Figure 5. SEM microtopography; (a) Ti6Al4V; (b) TiC/graphene/Ti6Al4V.

3.2. High-Temperature Performance

Figure 6 shows the engineering tensile strength of the LPBF-formed Ti6Al4V and TiC/graphene/Ti6Al4V composite at 400 °C, 500 °C, and 600 °C. At 400 °C, the tensile strengths of the Ti6Al4V alloy and composite were 880 MPa and 1006 MPa, respectively, which was 126 MPa higher than that of the Ti6Al4V alloy. At 500 °C, the tensile strengths of the Ti6Al4V alloy and composite were 806 MPa and 162 MPa higher than that of the Ti6Al4V alloy, respectively. At 600 °C, the tensile strengths of the Ti6Al4V alloy and composite were 462 MPa and 76 MPa higher than that of the Ti6Al4V alloy, respectively.

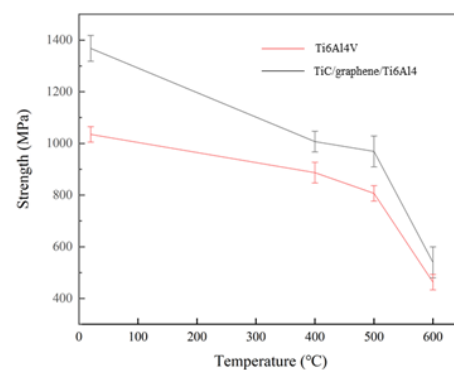


Figure 6. Tensile strength at different temperatures.

Figure 7 shows the fractographic morphology at the same temperature for both materials, with an increase in the dissociation surface area of the TiC/graphene/Ti6Al4V composites at a fractographic morphology of 400 °C and the formation of fewer pores during the drawing of the Ti6Al4V alloy. The area of the dissociation surface of both materials fractured at 500 °C decreased compared to that at 400 °C, but the number of pores with a fracture morphology at 500 °C increased in the composite compared to that in the Ti6Al4V alloy, while the size of the pores decreased. The fracture appearances of the two materials differed greatly at 600 °C, and the pore size and number of Ti6Al4V alloy were larger than that of the composite material because the softening behavior of the Ti6Al4V alloy at 600 °C was increased as well as the number of holes in the fracture appearances of the alloy. However, the composites contained reinforcement relative to the material; thus, the size and number of holes in the composite were smaller than those in the Ti6Al4V alloy, and the reinforcement phase effect was also reflected in the fracture morphology at 400 °C and 500 °C.

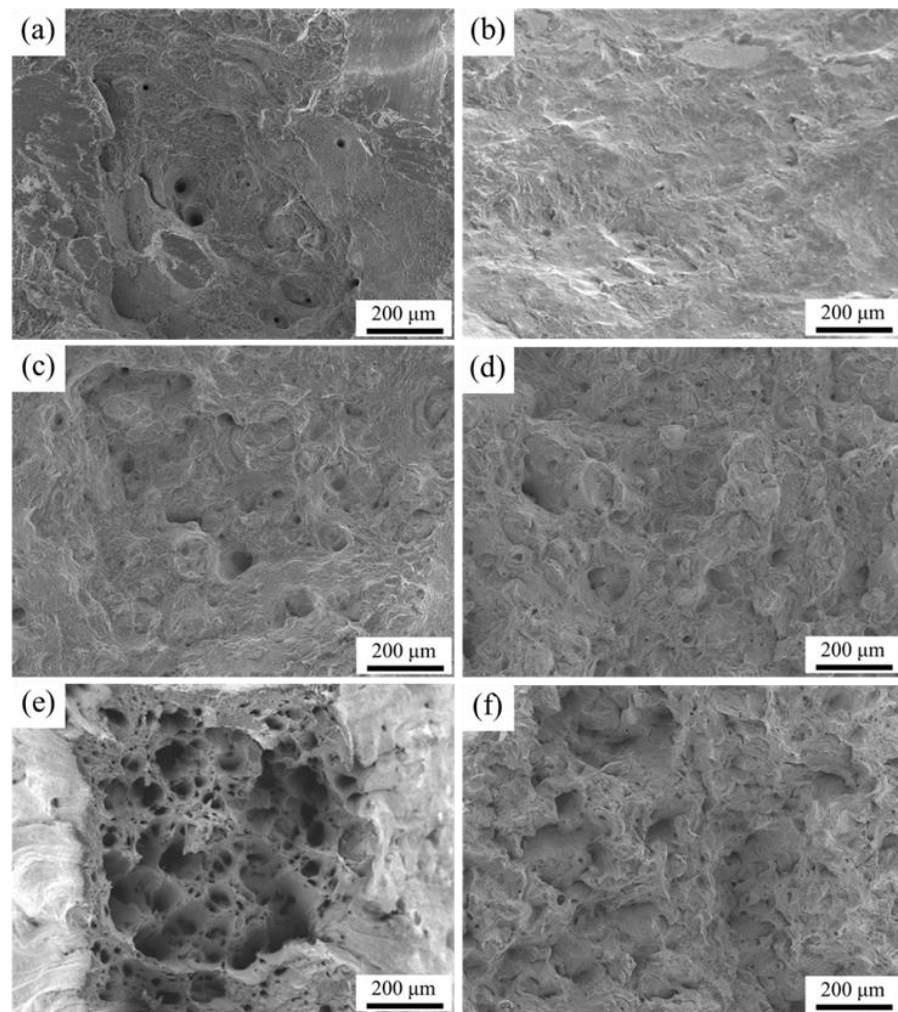


Figure 7. Fracture morphologies at different temperatures: (a,c,e) fracture morphologies of Ti6Al4V alloys at 400 °C, 500 °C, and 600 °C; (b,d,f) fracture morphologies of TiC/graphene/Ti6Al4V composite at 400 °C, 500 °C, and 600 °C.

Further analysis of the fracture mechanism of materials at high temperatures was carried out using micromorphology. The tensile fracture morphology of the Ti6Al4V alloy at 400 °C is shown in Figure 8a, with an average size of statistical dimple of 4.5 μm. The dimples, tear edges on the outside of the dimples, and a large step-like dissociation surface indicate that the Ti6Al4V alloy underwent both a ductile fracture and a brittle fracture at 400 °C. The dimple size of the Ti6Al4V alloy in the fracture morphology at 500 °C was counted, and the average dimple size was 4.2 μm; the dimple characteristics are similar to those of the fracture at 400 °C. The fracture morphology of the high-resolution SEM at 600 °C is shown in Figure 8c,d. The morphology inside the hole is also a dimple, with an average statistical dimple size of 0.6 μm.

The reason that the fracture morphology at 400 °C contained a large dissociation surface was that the Ti6Al4V alloy is mainly composed of α phase, which has a hexagonal structure, there are fewer slip systems in the phase, and the energy required for the dislocation slip is higher. In the fracture morphology at 500 °C, the reason for the reduction of the dissociation surface is mainly that the temperature increase provided more energy for the slip system to start easier; therefore, the dissociation surface was reduced. The formation of dimples is mainly due to the growth, aggregation, and fracture of micro-voids generated inside the alloy during the deformation. The micro-cavities of most alloys are formed at the second phase particles, while the Ti6Al4V alloy is a two-phase alloy, and the content of the phase structure is very small; therefore, the micro-cavities of the Ti6Al4V

alloy were mainly formed at the grain boundary [28]. With the increase in the tensile temperature, the proportion of dimples in the fracture morphology increased significantly. The reason for this is also that the energy of the externally supplied material increases with increasing temperature, making the dislocation more prone to slip. Slipping at a large number of dislocations accelerates the growth, aggregation, and fracture of the micro-voids, resulting in a larger void size as shown in Figure 7, reducing the size of the dimples, and decreasing the tensile strength of the Ti6Al4V alloy with increasing temperature.

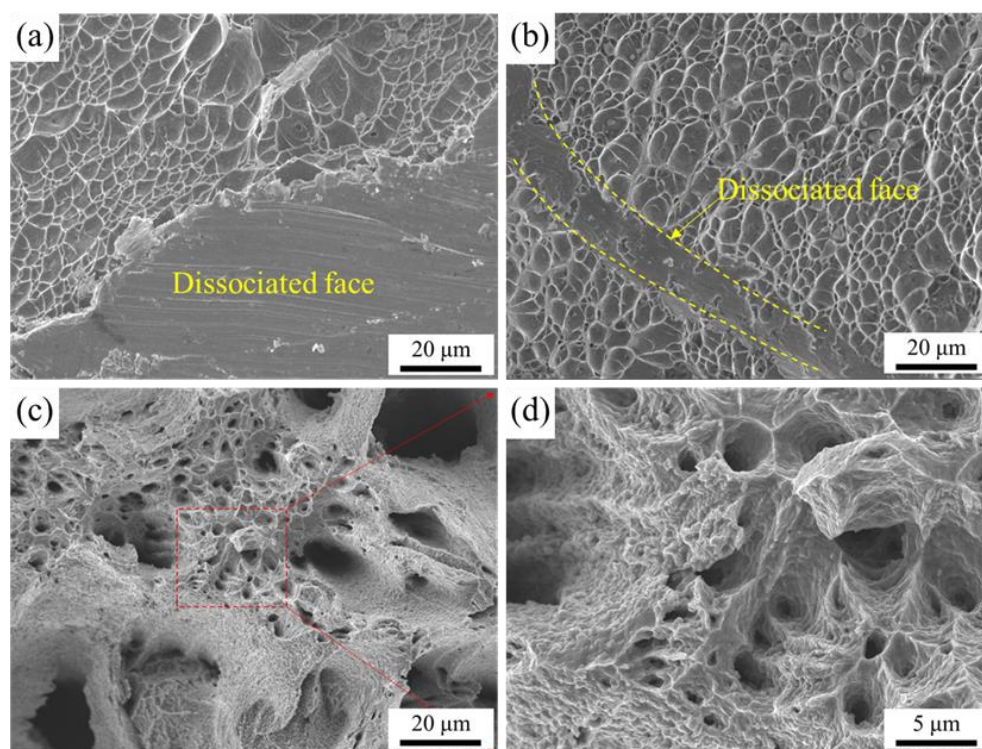


Figure 8. The high-temperature tensile fracture image of the Ti6Al4V alloy: (a) Fracture morphology at 400 °C; (b) fracture morphology at 500 °C; (c,d) Fracture morphology at 600 °C.

The fracture shape of the TiC/graphene/Ti6Al4V composite at 400 °C is shown in Figure 9a. Large cracks and a large number of dissociation surfaces are visible. The large cracks revealed a ‘u’ shape; at the same time, the sheet structure in the hole shown in Figure 9b–e, enlarged sheet structure of Figure 9e, and EDS surface sweep elemental analysis showed that the lamellar structure consisted of carbon elements as shown in Figure 9f. Therefore, the lamellar structure is unreacted graphene. The fracture morphology on both sides of the hole was different: one side was the dissociation surface, and the other side was the dimple (the average size of statistical dimples is 1.1 μm), as shown in Figure 9b. The fracture morphology of the TiC/graphene/Ti6Al4V composite at 500 °C shows a large number of dimples (average size of 0.97 μm) and a small amount of dissociation surface, while the dimple size of the TiC/graphene/Ti6Al4V composite is significantly reduced, and the dissociation surface is smaller than that of the Ti6Al4V alloy. The same sheet structure as that shown in Figure 9 existed in the holes, as shown in Figure 10c, and the composite of the sheet structure was carbon, as confirmed by an EDS surface scanning analysis. Therefore, this sheet structure was unreacted graphene in the composite. The fracture morphology of the TiC/graphene/Ti6Al4V composite at 600 °C was also the same as that of the Ti6Al4V alloy in Figure 10f, and the number and size of the pores were much smaller than those of the Ti6Al4V alloy, evidenced by the statistical dimple size average of 0.54 μm.

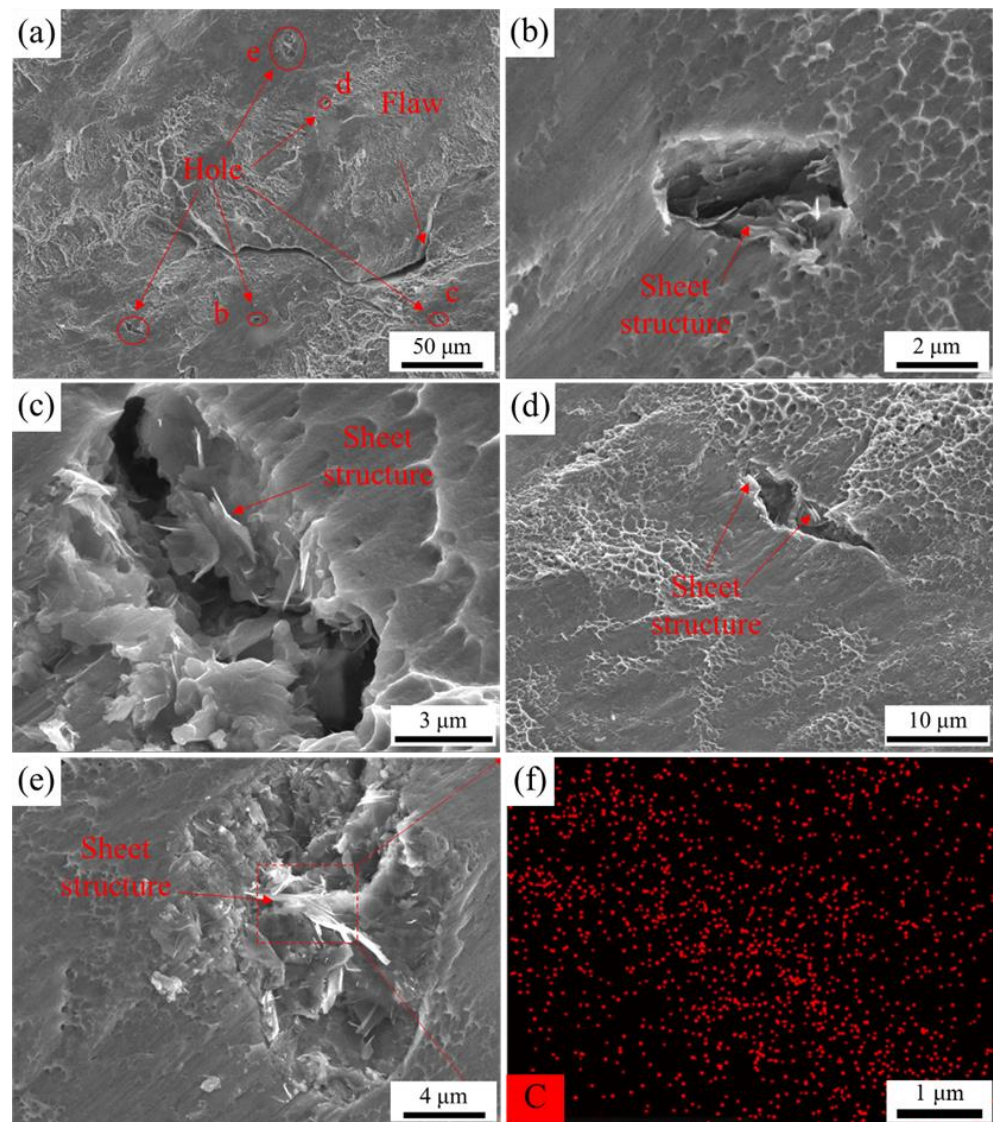


Figure 9. High-temperature tensile fracture of the TiC/graphene/Ti6Al4V composite: (a) 400 °C fracture; (b–f) enlarged morphology of b–f in (a); (f) distribution of element C in the selected area of ©.

By comparing the average dimple size of the Ti6Al4V alloy mentioned above, the dimple size of the TiC/graphene/Ti6Al4V composite material is significantly smaller at the same temperature. The decrease in dimple size is related to the grain refinement, which improves the performance of the material and precipitation of the composite material. The size of fracture dimples of both materials decreased gradually from 400–600 °C because the dislocation slip accelerates with the increase in temperature, and the growth, aggregation, and fracture speed of micro-voids increases, which leads to the decrease in dimple size and performance with the increase in temperature.

Graphene can be retained during LPBF by repeated rapid material melting and curing cycles. In addition, when a dislocation slip occurs, graphene prevents the dislocation slip and enhances the properties of the composite [29]. It was inferred from the above that the micro-cavities of the Ti6Al4V alloy were easy to form at the grain boundary and second phase particles. Therefore, the formation of voids with graphene also proves that, during the deformation, the micro-voids are easy to form together by precipitation and break with the growth and aggregation of micro-voids, as shown in Figures 9 and 10. The TiC in the TiC/graphene/Ti6Al4V composites was produced by an in situ reaction of graphene and Ti,

as shown in Figure 3. The TiC particles enhanced the properties of the composite through the Orowan strengthening mechanism [30]. At the same time, nano-scale TiC particles were distributed in the composite matrix, which played a role in passivating the crack tip, delaying the crack growth [31], and enhancing the tensile properties of the composite. Thus, both the TiC particles and the graphene in the TiC/graphene/Ti6Al4V composite improved the tensile strength of the composite, making the tensile strength of the composite higher than that of the Ti6Al4V alloy at 400 °C, 500 °C, and 600 °C.

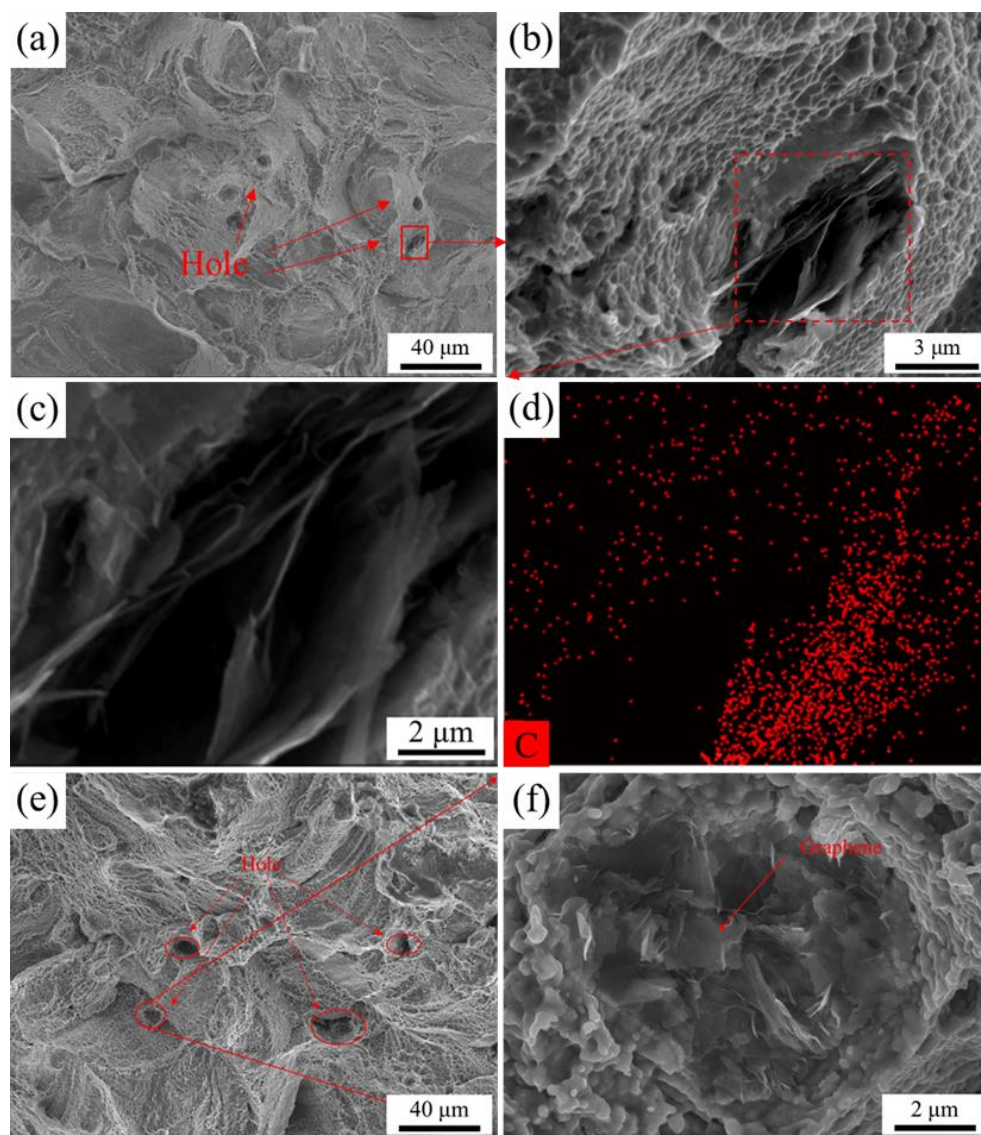


Figure 10. High-temperature tensile fracture of the TiC/graphene/Ti6Al4V composite: (a) fracture at 500 °C; (b) enlarged view of Figure (a); (c) enlarged view of (b); (d) the distribution of C elements on EDS surface of (c); (e,f) fracture morphology at 600 °C.

The microhardness of the Ti6Al4V alloy and TiC/graphene/Ti6Al4V composite formed by LPBF at room temperature and high temperatures is shown in Figure 11. The hardness of the two materials decreased step by step at high temperatures. The microhardness of the Ti6Al4V alloy at room temperature was 336 HV, and that formed by electron beam was 340 HV [32], whereas the microhardness of the TiC/graphene/Ti6Al4V composite was 419 HV, which was 83 HV higher than the LPBF-formed Ti6Al4V alloy and 79 HV higher than the Ti6Al4V alloy formed by the electron beam. The micro-hardness of the TiC/graphene/Ti6Al4V composite at 400 °C, 500 °C, and 600 °C was 70 HV,

59 HV, and 61 HV higher than that of the TiC/graphene/Ti6Al4V composite, respectively. The microhardness of the TiC/graphene/Ti6Al4V composite at 600 °C was higher than that of the Ti6Al4V alloy at 400 °C, indicating that the working temperature of the TiC/graphene/Ti6Al4V composite could be higher than that of the Ti6Al4V alloy. The hardness of the TiC/graphene/Ti6Al4V composite could be improved by the grain size refinement of the composite and dispersion strengthening mechanism of the TiC particles and graphene.

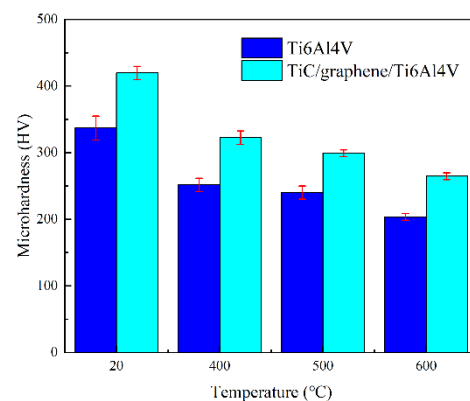


Figure 11. Microhardness of Ti6Al4V and TiC/graphene/Ti6Al4V alloys at room temperature and high temperatures.

4. Conclusions

In this study, the microstructure and high-temperature mechanical properties of Ti6Al4V and TiC/graphene/Ti6Al4V composites formed using LPBF were investigated and compared. The following conclusions were obtained:

(1) During the LPBF, graphene reacted with Ti in situ to form TiC particles, which were homogeneously distributed between α' acicular martensite; the addition of graphene refined the size of acicular α' martensite. At the same time, the graphene and the TiC particles played the role of dispersion strengthening, and the mechanical properties of the TiC/graphene/Ti6Al4V composite were improved by the combination of the fine-grain strengthening mechanism and the dispersion strengthening mechanism.

(2) The density of the Ti6Al4V alloy was 99.2% and that of the TiC/graphene/Ti6Al4V composite was 98.9%. However, a density above 98% has little influence on its mechanical properties [27].

(3) The high-temperature tensile strength of the TiC/graphene/Ti6Al4V composite sample was 126 MPa, 162 MPa, and 76 MPa higher than that of the Ti6Al4V material sample at 400 °C, 500 °C, and 600 °C, respectively.

(4) The addition of graphene refined the needle shape α' martensite size, while the average dimple size of the composite at the same temperature was smaller than that of the Ti6Al4V alloy. Graphene can be retained during LPBF by repeated rapid material melting and curing cycles, with microscopic voids formed during high-temperature tension.

(5) The microhardness of the TiC/graphene/Ti6Al4V composite at room temperature, 400 °C, 500 °C, and 600 °C was 82 HV, 70 HV, 59 HV, and 61 HV higher than that of the Ti6Al4V alloy, respectively.

Author Contributions: Conceptualization, Z.Z. and S.C.; methodology, S.C.; software, S.C.; validation, Z.Z., P.B. and W.D.; writing—original draft preparation, S.C.; writing—review and editing, Z.Z., P.B. and W.D.; supervision, Z.Z. All authors have read and agreed to the published version of the manuscript.

Funding: The authors would like to thank the National Natural Science Foundation of China (51775521, U22A20192), the Key Research and Development Project of Shanxi Province (201903D121009), Scientific and Technological Innovation Programs of Higher Education Institutions in Shanxi, Equipment Pre-research Field Fund, China (No.61400040208).

Data Availability Statement: The data presented in this study are presented in Figures and tables in this article.

Conflicts of Interest: The authors declare no conflict of interest.

References

1. Zhao, Z.; Zhang, L.; Bai, P.; Du, W.; Wang, S.; Xu, X.; Dong, Q.; Li, Y.; Han, B. Tribological Behavior of In Situ TiC/Graphene/Graphite/Ti6Al4V Matrix Composite Through Laser Cladding. *Acta Metall. Sin. Engl. Lett.* **2021**, *34*, 1317–1330. [[CrossRef](#)]
2. Christoph Leyens, M.P. *Titanium and Titanium Alloys: Fundamentals and Applications*; Chemical Industry Press: Beijing, China, 2003.
3. Zhou, Z.; Liu, Y.; Liu, X.; Zhan, Q.; Wang, K. Microstructure evolution and mechanical properties of in-situ Ti6Al4V–TiB composites manufactured by selective laser melting. *Compos. Part B Eng.* **2021**, *207*, 108567. [[CrossRef](#)]
4. Zhao, Z.; Bai, P.; Du, W.; Liu, B.; Pan, D.; Das, R.; Liu, C.; Guo, Z. An overview of graphene and its derivatives reinforced metal matrix composites: Preparation, properties and applications. *Carbon* **2020**, *170*, 302–326. [[CrossRef](#)]
5. Yu, C.; Liu, X.; Li, Y.; Song, C.; Ma, G.; Niu, F.; Wu, D. Investigations of the microstructure and performance of TiCp/Ti6Al4V composites prepared by directed laser deposition. *Int. J. Mech. Sci.* **2021**, *205*, 106595. [[CrossRef](#)]
6. Liang, X.; Liu, Z.; Wang, B. Physic-chemical analysis for high-temperature tribology of WC-6Co against Ti-6Al-4V by pin-on-disc method. *Tribol. Int.* **2020**, *146*, 106242. [[CrossRef](#)]
7. Zhang, W.; Wang, M.; Chen, W.; Feng, Y.; Yu, Y. Preparation of TiBw/Ti-6Al-4V composite with an inhomogeneous reinforced structure by a canned hot extrusion process. *J. Alloys Compd.* **2016**, *669*, 79–90. [[CrossRef](#)]
8. Yang, M.; Liu, Y.; Fan, T.; Zhang, D. Metal-graphene interfaces in epitaxial and bulk systems: A review. *Prog. Mater. Sci.* **2020**, *110*, 100652. [[CrossRef](#)]
9. Guo, Y.; Yu, K.; Niu, J.; Sun, M.; Dai, G.; Sun, Z.; Chang, H. Effect of reinforcement content on microstructures and mechanical properties of graphene nanoflakes-reinforced titanium alloy matrix composites. *J. Mater. Res. Technol.* **2021**, *15*, 6871–6882. [[CrossRef](#)]
10. Waqar, S.; Sun, Q.; Liu, J.; Guo, K.; Sun, J. Numerical investigation of thermal behavior and melt pool morphology in multi-track multi-layer selective laser melting of the 316L steel. *Int. J. Adv. Manuf. Technol.* **2020**, *112*, 879–895. [[CrossRef](#)]
11. Waqar, S.; Guo, K.; Sun, J. FEM analysis of thermal and residual stress profile in selective laser melting of 316L stainless steel. *J. Manuf. Process.* **2021**, *66*, 81–100. [[CrossRef](#)]
12. Ahmed Obeidi, M.; Uí Mhurchadha, S.M.; Raghavendra, R.; Conway, A.; Souto, C.; Tormey, D.; Ahad, I.U.; Brabazon, D. Comparison of the porosity and mechanical performance of 316L stainless steel manufactured on different laser powder bed fusion metal additive manufacturing machines. *J. Mater. Res. Technol.* **2021**, *13*, 2361–2374. [[CrossRef](#)]
13. Korkmaz, M.E.; Waqar, S.; Garcia-Collado, A.; Gupta, M.K.; Krolczyk, G.M. A technical overview of metallic parts in hybrid additive manufacturing industry. *J. Mater. Res. Technol.* **2022**, *18*, 384–395. [[CrossRef](#)]
14. Korkmaz, M.E.; Gupta, M.K.; Waqar, S.; Kuntoğlu, M.; Krolczyk, G.M.; Maruda, R.W.; Pimenov, D.Y. A short review on thermal treatments of Titanium & Nickel based alloys processed by selective laser melting. *J. Mater. Res. Technol.* **2022**, *16*, 1090–1101.
15. Korkmaz, M.E.; Gupta, M.K.; Robak, G.; Moj, K.; Krolczyk, G.M.; Kuntoğlu, M. Development of lattice structure with selective laser melting process: A state of the art on properties, future trends and challenges. *J. Manuf. Process.* **2022**, *81*, 1040–1063. [[CrossRef](#)]
16. Grasso, M.; Colosimo, B.M. Process defects and in situ monitoring methods in metal powder bed fusion: A review. *Meas. Sci. Technol.* **2017**, *28*, 044005. [[CrossRef](#)]
17. Vilaro, T.; Colin, C.; Bartout, J.D. As-Fabricated and Heat-Treated Microstructures of the Ti-6Al-4V Alloy Processed by Selective Laser Melting. *Metall. Mater. Trans. A* **2011**, *42*, 3190–3199. [[CrossRef](#)]
18. Panwisawas, C.; Qiu, C.L.; Sovani, Y.; Brooks, J.W.; Attallah, M.M.; Basoalto, H.C. On the role of thermal fluid dynamics into the evolution of porosity during selective laser melting. *Scr. Mater.* **2015**, *105*, 14–17. [[CrossRef](#)]
19. Majeed, A.; Zhang, Y.; Ren, S.; Lv, J.; Peng, T.; Waqar, S.; Yin, E. A big data-driven framework for sustainable and smart additive manufacturing. *Robot. Comput. Integr. Manuf.* **2021**, *67*, 102026. [[CrossRef](#)]
20. Zhao, Z.; Bai, P.; Misra, R.D.K.; Dong, M.; Guan, R.; Li, Y.; Zhang, J.; Tan, L.; Gao, J.; Ding, T.; et al. AlSi10Mg alloy nanocomposites reinforced with aluminum-coated graphene: Selective laser melting, interfacial microstructure and property analysis. *J. Alloys Compd.* **2019**, *792*, 203–214. [[CrossRef](#)]
21. Wang, Y.C.; Shi, J.; Lu, S.Q.; Wang, Y. Selective Laser Melting of Graphene-Reinforced Inconel 718 Superalloy: Evaluation of Microstructure and Tensile Performance. *J. Manuf. Sci. Eng. Trans. Asme* **2017**, *139*, 4. [[CrossRef](#)]
22. Huo, P.; Zhao, Z.; Du, W.; Zhang, Z.; Bai, P.; Tie, D. Deformation strengthening mechanism of in situ TiC/TC4 alloy nanocomposites produced by selective laser melting. *Compos. Part B Eng.* **2021**, *225*, 109305. [[CrossRef](#)]
23. Huo, P.; Zhao, Z.; Du, W.; Bai, P. Deformation and fracture mechanisms of in situ synthesized TiC reinforced TC4 matrix composites produced by selective laser melting. *Ceram. Int.* **2021**, *47*, 19546–19555. [[CrossRef](#)]
24. Zhao, Z.Y.; Li, L.; Bai, P.K.; Jin, Y.; Wu, L.Y.; Li, J.; Guan, R.G.; Qu, H.Q. The Heat Treatment Influence on the Microstructure and Hardness of TC4 Titanium Alloy Manufactured via Selective Laser Melting. *Materials* **2018**, *11*, 1318. [[CrossRef](#)] [[PubMed](#)]

25. Zhao, Z.; Wang, S.; Du, W.; Bai, P.; Zhang, Z.; Wang, L.; Wang, J.; Tie, D. Interfacial structures and strengthening mechanisms of in situ synthesized TiC reinforced Ti6Al4V composites by selective laser melting. *Ceram. Int.* **2021**, *47*, 34127–34136. [[CrossRef](#)]
26. Wang, S.; Zhao, Z.; Bai, P.; Du, W.; Li, L. Effect of in situ synthesis TiC on the microstructure of graphene/Ti6Al4V composite fabricated by selective laser melting. *Mater. Lett.* **2021**, *304*, 130715. [[CrossRef](#)]
27. Wang, H.; Fang, Z.Z.; Sun, P. A critical review of mechanical properties of powder metallurgy titanium. *Int. J. Powder Metall.* **2010**, *46*, 45–57.
28. Xiao, M.; Colida.; Lai, C.; Dou, E.; Du, L. SLM Formed TC4 Titanium Alloy High Temperature Tensile Mechanical Properties and Fracture Mechanism Analysis. *Appl. Laser* **2021**, *41*, 350–356.
29. Kim, Y.; Lee, J.; Yeom, M.S.; Shin, J.W.; Kim, H.; Cui, Y.; Kysar, J.W.; Hone, J.; Jung, Y.; Jeon, S.; et al. Strengthening effect of single-atomic-layer graphene in metal-graphene nanolayered composites. *Nat. Commun.* **2013**, *4*, 2114. [[CrossRef](#)]
30. Zhang, X.; Song, F.; Wei, Z.; Yang, W.; Dai, Z. Microstructural and mechanical characterization of in-situ TiC/Ti titanium matrix composites fabricated by graphene/Ti sintering reaction. *Mater. Sci. Eng. A* **2017**, *705*, 153–159. [[CrossRef](#)]
31. Hu, Z.-Y.; Cheng, X.-W.; Li, S.-L.; Zhang, H.-M.; Wang, H.; Zhang, Z.-H.; Wang, F.-C. Investigation on the microstructure, room and high temperature mechanical behaviors and strengthening mechanisms of the (TiB + TiC)/TC4 composites. *J. Alloys Compd.* **2017**, *726*, 240–253. [[CrossRef](#)]
32. Baufeld, B.; Brandl, E.; van der Biest, O. Wire based additive layer manufacturing: Comparison of microstructure and mechanical properties of Ti-6Al-4V components fabricated by laser-beam deposition and shaped metal deposition. *J. Mater. Process. Technol.* **2011**, *211*, 1146–1158. [[CrossRef](#)]

Disclaimer/Publisher’s Note: The statements, opinions and data contained in all publications are solely those of the individual author(s) and contributor(s) and not of MDPI and/or the editor(s). MDPI and/or the editor(s) disclaim responsibility for any injury to people or property resulting from any ideas, methods, instructions or products referred to in the content.